Bound States in the Continuum as Nodal Chain Points of Scattering Matrices

Wenzhe Liu,[1,2,3,*,†] Yuan-Song Zeng,[4,†] Jingyi Zhao,[1,2,†] Chenfeng Yang,[4] Ruo-Yang Zhang,[3] Xiaohan Cui,[3] Geng-Bo Wu,[4,‡] and C. T. Chan[3,§]

[1]*Institute for Nanoelectronic Devices and Quantum Computing, Fudan University, Songhu Road, Yangpu District, Shanghai 200438, China*

[2]*State Key Laboratory of Surface Physics, Key Laboratory of Micro- and Nano-Photonic Structures (Ministry of Education), and Department of Physics, Fudan University, Songhu Road, Yangpu District, Shanghai 200438, China*

[3]*Department of Physics and Institute for Advanced Study, The Hong Kong University of Science and Technology, Clear Water Bay, Kowloon, Hong Kong 999077, China*

[4]*State Key Laboratory of Terahertz and Millimeter Waves and Department of Electrical Engineering, City University of Hong Kong, Tat Chee Avenue, Kowloon, Hong Kong 999077, China*

(Received 3 April 2025; revised 30 October 2025; accepted 19 November 2025; published 11 December 2025)

Bound states in the continuum (BICs), exotic resonances with infinite lifetimes embedded in radiation continua, have long been studied for their topological robustness. Meanwhile, nodal lines—degenerate momentum-space manifolds in photonic and electronic band structures—represent another cornerstone of topological physics. Here, we unveil a profound connection between these phenomena by demonstrating that BICs act as topological chain points pinning together nodal lines within scattering-matrix eigenvalue space. Through scattering-matrix eigenphase analysis, we show that BICs enforce robust nodal chain formation in frequency-momentum space, even when system symmetries are broken. Experimentally, we validate this mechanism using a metasurface platform, where angle-resolved phase measurements reveal nodal lines intersecting at a symmetry-protected BIC. Strikingly, breaking mirror symmetry preserves the BIC-pinned nodal chain, highlighting its origin in the intrinsic singular scattering nature of BICs rather than conventional symmetry protection. This Letter establishes scattering matrices as a natural framework to unify BICs and nodal topology, offering new pathways to engineer topologically robust photonic systems resilient to perturbations. Our findings bridge fundamental concepts in topological photonics and open avenues for applications in metasurfaces and light-matter interaction control.

DOI: 10.1103/rpb2-ryyk

Introduction—Bound states in the continuum (BICs) are nonradiative states whose confinement stems from their fundamental topological nature despite existing within radiating mode continua [1–13]. This topological protection manifests in momentum-space eigenpolarizations, where BICs serve as polarization vortex centers carrying topological charges [14–21]. These properties enable spin-orbit interactions, leading to phenomena such as optical vortex generation and beam shifting [20,22,23]. The robust nature of these singular features makes them valuable for designing photonic devices maintaining functionality despite structural imperfections.

In parallel, nodal lines—continuous band degeneracies characterized by linear crossings (diabolic points, DPs [24–26])—have emerged as fundamental topological features in Hamiltonian matrices describing electronic and photonic band structures [25,27–36]. These lines naturally form nodal chains in systems with specific symmetries, revealing rich topological structures. While both BICs and nodal lines have been extensively studied separately, their potential connection through scattering processes remains unexplored.

In this Letter, we reveal a striking connection between BICs and nodal lines within the scattering matrix—a fundamental tool for describing light-structure interactions [37,38]. By analyzing scattering matrix eigenvalues, we discover that BICs act as chain points pinning together nodal lines, forming robust nodal chains in frequency-momentum space. Through experimental measurements on a reflective metasurface with required symmetries, we validate this previously unrecognized aspect of BIC topology in scattering processes. Remarkably, the nodal chain pinning persists even when mirror symmetry is broken, demonstrating that its robustness stems not from simple

*Contact author: wzliu@fudan.edu.cn

†These authors contributed equally to this work.

‡Contact author: bogwu2@cityu.edu.hk

§Contact author: phchan@ust.hk

symmetry protection but from the intrinsic singular characteristic of BICs. These findings uncover a deeper connection between BICs and scattering processes, opening new avenues for controlling light-matter interactions through topologically protected features.

Results—Theoretical description of nodal lines in scattering matrices: We begin with lossless reflective metasurface structures terminated by perfect mirrors. Such systems are fully described by 2×2 scattering matrices, as mirror substrates eliminate transmission channels and material loss absence ensures energy conservation (unitarity of scattering matrix). This provides an ideal platform to study the essential physics. The scattering matrix entries are complex reflection coefficients r_{ij}, where i and j denote polarization states parallel (p) and perpendicular (s) to the incidence plane: $S(\omega, \mathbf{k}_\parallel) = \begin{pmatrix} r_{pp} r_{ps} \\ r_{sp} r_{ss} \end{pmatrix}$. Fundamental symmetries constrain these entries [37–39]. For example, with C_2 symmetry and Lorentz reciprocity, antidiagonal entries must be equal:

$$r_{ji} = r_{ij}. \tag{1}$$

Further with time-reversal symmetry:

$$\begin{aligned} r_{pp} r_{ps}^* + r_{ps} r_{ss}^* &= 0, \\ r_{pp} r_{pp}^* + r_{sp} r_{sp}^* = r_{ss} r_{ss}^* + r_{ps} r_{ps}^* &= 1. \end{aligned} \tag{2}$$

As a result, the full scattering matrix is expressed by three real parameters $a \in [0, 1]$, $\phi_1, \phi_2 \in [0, 2\pi)$:

$$\begin{aligned} r_{ss} &= -a e^{i\phi_1}, \quad r_{ps} = r_{sp} = \sqrt{1-a^2}\, e^{i\phi_2}, \\ r_{pp} &= a e^{i(2\phi_2 - \phi_1)}, \\ S &= \begin{pmatrix} a e^{i(2\phi_2-\phi_1)} & \sqrt{1-a^2}\, e^{i\phi_2} \\ \sqrt{1-a^2}\, e^{i\phi_2} & -a e^{i\phi_1} \end{pmatrix}. \end{aligned} \tag{3}$$

Detailed derivations showing how these symmetry constraints lead to the three-parameter form appear in Supplemental Material [40]. This parametrization automatically enforces unitarity due to energy conservation in lossless system. The eigenvectors ν will be

$$\begin{aligned} \nu &= \nu_0 e^{i\varphi}, \\ \nu_0(\omega, k_x, k_y) &= \Big(-a \cos(\phi_2 - \phi_1) \\ &\quad \pm \sqrt{1 - a^2 \sin^2(\phi_2 - \phi_1)}, \sqrt{1-a^2} \Big)^{\mathrm{T}}, \end{aligned} \tag{4}$$

where φ is arbitrary phase.

The eigenvector $\nu = \nu_0 e^{i\varphi}$ describes a polarization state, where overall phase $e^{i\varphi}$ is physically irrelevant. Physical content resides entirely in the real vector ν_0, specifying a "linear polarization orientation" in the s-p plane. Since linear polarization is defined only by orientation (not direction), states differing by 180° are identical. Mathematically, the "linear-polarization-orientation space" is topologically equivalent to circle S^1 (or real projective line $\mathbb{RP}^1$), with fundamental group $\pi_1(S^1) = \mathbb{Z}$. This integer group characterizes how many times polarization orientation winds by π traversing a closed path in frequency-momentum space, with each integer corresponding to topologically distinct winding configurations. Such configurations necessitate singularities—points where eigenvector orientation becomes ill-defined due to eigenvalue degeneracy. The simplest nontrivial case corresponds to single π winding (winding number ± 1), where ν returns to itself up to sign after traversing the path, corresponding to a DP. One can then conclude that, protected by combined C_2 symmetry, reciprocity, and time-reversal symmetry, nodal lines formed by DPs naturally arise and robustly exist in frequency-momentum space. Such a line is the "extrusion" of DPs into three-dimensional parameter space [29].

Scattering-matrix nodal chains and BICs: Additional symmetries can constrain nodal lines to specific subspaces in frequency-momentum space, potentially forming nodal chains. For example, mirror symmetries "lock" these robust nodal lines onto mirror planes [41]. In systems with intersecting mirror planes (e.g., C_{2v}-symmetric structures), nodal lines on these planes can form configurations with crossing points as "chain points." When these symmetries are broken, such nodal chains (like those found in Hamiltonian systems) generally split into separate nodal lines in the 3D frequency-momentum space.

Interestingly, we discover a special class of robust nodal chains pinned by BICs, as illustrated in Fig. 1(b). This pinning mechanism persists when mirror symmetries break, though we best understand its origin by first examining eigenvalue structure in mirror-symmetric systems. As the scattering matrix is unitary, its eigenvalues are constrained to the complex unit circle, and we gain clear physical insight examining their phases (eigenphases). When the in-plane wave vector of the considered scattering process lies in mirror-symmetric directions (e.g., $k_x = 0$ or $k_y = 0$), eigenscattering channels separate by different mirror parities (corresponding to x- or y-polarized modes). For regular resonances with such mirror-symmetric in-plane wave vectors, the eigenphase in its eigenscattering channel exhibits smooth 2π phase change as scattering frequency ω traverses its eigenfrequency, with a change rate proportional to the bandwidth, as shown in Fig. 1(a) (top panel). A BIC represents the limiting case where bandwidth approaches zero, resulting in a sudden 2π phase jump at BIC frequency ω_{BIC} (Fig. 1, bottom panel). This 2π phase jump, while mathematically trivial in the cyclic eigenphase space of unitary scattering matrices (as $2\pi \equiv 0$), represents a unique topological feature impossible in Hamiltonian systems where eigenvalues span unbounded ranges.

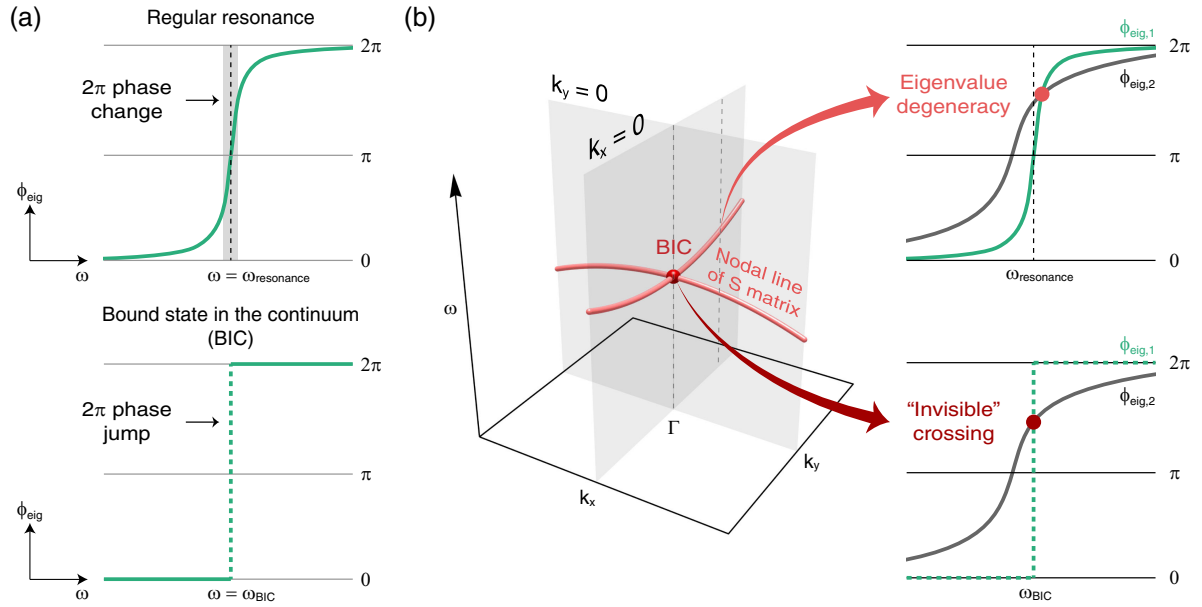

FIG. 1. Behavior of scattering matrix eigenvalues and interaction between nodal lines and bound states in the continuum (BICs). (a) Phase behavior of eigenmodes in reflective systems with mirror symmetry. For regular resonances (top) with a mirror symmetric incident wave vector, the eigenphase in the eigenscattering channel ϕ_{eig} exhibits smooth 2π phase change as frequency ω traverses the resonance. In contrast, a bound state in the continuum (BIC, bottom) introduces a sudden 2π phase jump at BIC frequency ω_{BIC} due to zero decay ratio and bandwidth. This phase jump appears mathematically trivial (as $2\pi \equiv 0$), but its significance becomes clear in 3D frequency-momentum space. (b) Effects of BICs on the eigenvalue structure and connection to scattering-matrix nodal lines. The left panel shows 3D frequency-momentum space with nodal lines (light red) corresponding to symmetry-protected eigenvalue degeneracies. The BIC (dark red) acts as a "chain point" where two nodal lines intersect. Right panels show phase behavior of eigenvalues $\phi_{\mathrm{eig},1}$ and $\phi_{\mathrm{eig},2}$: at the Γ point (BIC location), the eigenvalue in the BIC's mirror-parity channel undergoes a sudden 2π jump. This jump crosses the orthogonal-channel eigenvalue, but this crossing is "invisible" due to the phase jump nature. Moving away from the Γ point (even infinitesimally) in mirror-symmetric directions ($k_x = 0$ or $k_y = 0$), the BIC becomes a regular resonance, and the sudden jump transitions to a smooth phase change, making the crossing a true mirror-symmetry-protected degeneracy point. Consequently, the BIC has a mirror-symmetry-protected nodal line pinned on it. Two intersecting mirror planes lead to two intersecting nodal lines with the BIC as chain point.

This distinctive scattering matrix behavior has profound implications in 3D frequency-momentum space.

Consider a BIC at the Γ point in frequency-momentum space. When the eigenphase in the BIC's mirror-parity channel undergoes this sudden 2π jump at the Γ point, it spans the complete eigenphase value range, inevitably intersecting the opposite-parity channel eigenphase. This crossing is "invisible" due to the 0-2π equivalence, as illustrated in Fig. 1(b) (top right). The crossing's true significance emerges moving away from Γ along mirror-symmetric directions. Even infinitesimal displacement transforms the BIC into a finite-bandwidth resonance with continuous phase evolution, making the crossing explicitly observable [Fig. 1(b), bottom right panel]. As we continue moving along the mirror-symmetric directions, this crossing traces a continuous line of mirror-symmetry-protected eigenvalue degeneracies, forming a nodal line pinned to the BIC. In systems with two intersecting mirror planes, this mechanism naturally gives two nodal lines intersecting at the BIC, which serves as a chain point in frequency-momentum space [Fig. 1(b), left panel].

Numerical demonstration of BIC-pinned nodal chains: We numerically analyzed a reflective metasurface structure using finite-element method (FEM) simulations (see Methods) to demonstrate our theoretical predictions about BIC-pinned nodal chains. The structure consists of a metallic layer etched with periodic long rectangular slots on a dielectric substrate (dielectric constant $\varepsilon_r = 6.15$, thickness $t = 0.635$ mm), backed by a metallic mirror [Fig. 2(a), inset]. The rectangular slots, each 3-mm wide and separated by 1.5-mm metallic strips, form a one-dimensional grating with period $a = 4.5$ mm. This configuration exhibits C_{2v} symmetry with two perpendicular mirror planes, providing necessary symmetry conditions for both BIC and nodal chain formations.

Figure 2(a) shows the eigenfrequency dispersion relation—the resonance frequency $\omega_{\mathrm{resonant}}$ of metastructure modes as a function of the in-plane wave vector (k_x, k_y)—represented by solid lines in frequency-momentum space. Shaded areas represent the decay ratio (bandwidth) of eigenresonances. In the lower band, the decay ratio vanishes at a specific point, indicating BIC

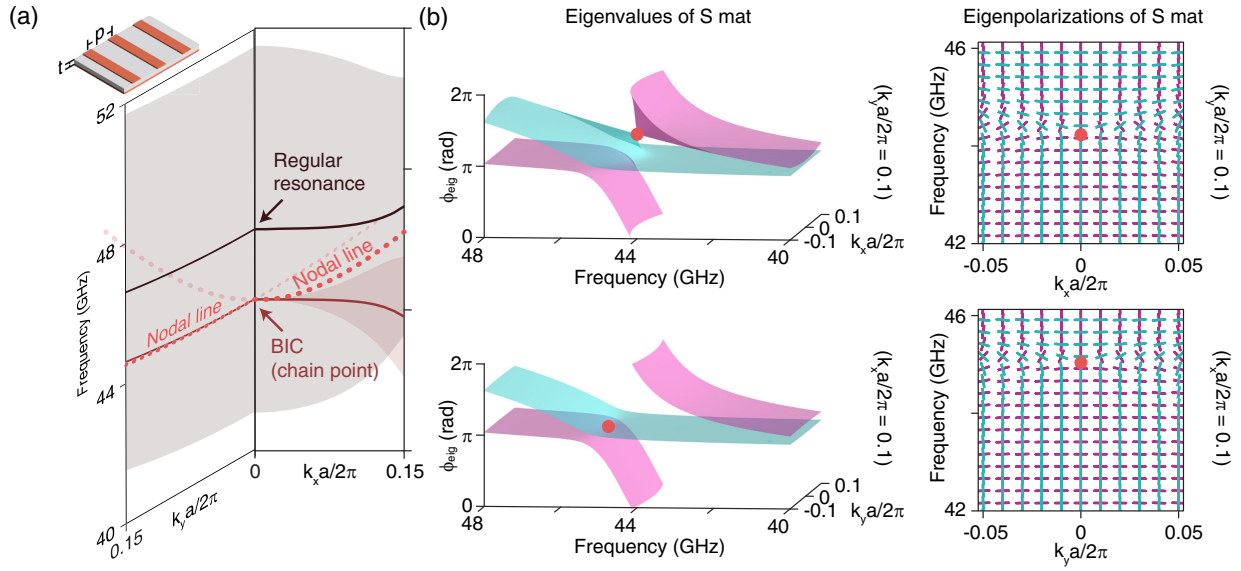

FIG. 2. Numerical demonstration of nodal chain phenomenon in a reflective metasurface structure. (a) Inset: schematic of simulated reflective metasurface structure, fabricated using a printed circuit board (PCB). The structure consists of metallic grating (etched with long rectangular slots) on a dielectric substrate, backed by a metallic mirror layer. The overall structure exhibits C_{2v} symmetry with two perpendicular mirror planes. The eigenfrequency dispersion relation in the frequency-momentum space (solid lines for k_x and k_y) results in two scattering-matrix-eigenvalue nodal lines (dashed lines) pinned at a BIC, forming a nodal chain. The BIC acts as a fixed point where nodal lines intersect, dictated by the system symmetry constraints. (b) Left: eigenvalue surfaces of scattering matrix, showing phase evolution of the two eigenvalues ϕ_{eig} in the frequency-momentum domain. The upper panel corresponds to the slice at $k_y a/2\pi = 0.1$, while the lower panel shows the slice at $k_x a/2\pi = 0.1$. In each momentum slice, a diabolic point (conical eigenvalue degeneracy) appears where the slice cuts through a nodal line. Right: eigenpolarization maps displaying scattering-matrix eigenvectors at the two momentum slices, visualized as polarization ellipses in the frequency-momentum space. Protected by fundamental symmetries, eigenpolarizations are all linear, and all ellipses become line segments. The colors of polarization ellipses correspond to the eigenvalue surfaces. Polarization vortices are clearly visible around the DPs.

presence. These dispersion curves, analyzed through scattering matrix formalism, give rise to two nodal lines in the scattering-matrix eigenvalue space (dashed lines) that intersect at this BIC point, demonstrating predicted chain-point behavior.

Scattering-matrix eigenvalue surfaces [Fig. 2(b), left panels] reveal the phase evolution of the two eigenvalues ϕ_{eig} in different momentum slices. At $k_y a/2\pi = 0.1$ (top) and $k_x a/2\pi = 0.1$ (bottom), we observe conical eigenvalue degeneracies, i.e., DPs, where respective momentum slices intersect nodal lines. These intersections provide direct evidence of the nodal chain structure pinned by the BIC.

The topology of these nodal lines becomes evident through scattering-matrix eigenvector examination. Right panels of Fig. 2(b) visualize these eigenvectors as line segments in the frequency-momentum space, with colors corresponding to the associated eigenvalue surfaces shown in left panels. Around each DP, we observe distinct vortex patterns where eigenvector orientation winds by π around the degeneracy point—precisely matching the topological charge predicted. These characteristic vortex patterns verify our theoretical framework and demonstrate nodal chain formation associated with BIC in the scattering-matrix eigenvalue space. To demonstrate this phenomenon's generality beyond metallic structures, we performed additional FEM simulations on all-dielectric metasurfaces with perfect-mirror substrates (see Supplemental Material [40]), confirming BIC-pinned nodal chains persist in dielectric systems.

Experimental verification of BIC-associated nodal chains: We fabricated the metasurface structure using printed circuit board (PCB) technology and performed angle-resolved phase measurements to verify nodal chain existence in scattering-matrix eigenvalue space. The sample consists of a 200×200 mm^2 Rogers RO3006 PCB board, both sides initially copper covered. Through selective etching on one side, we created a grating pattern within a central $\sim 135 \times 135$ mm^2 area, preserving the back copper layer as a mirror [inset of Fig. 3(a)].

The experimental setup [Fig. 3(a)] consists of a source and receiver positioned in a far-field region, two meters from the sample, housed in an anechoic chamber to minimize multipath effects. Wideband circular polarizers [42,43] are placed before the source and receiver antennas to achieve clockwise-incident and counterclockwise-received circular polarizations. The source and receiver positions were adjusted to achieve incident lifting angles θ_{inc} of 8°, 12°, and 16°. By rotating the sample mounting

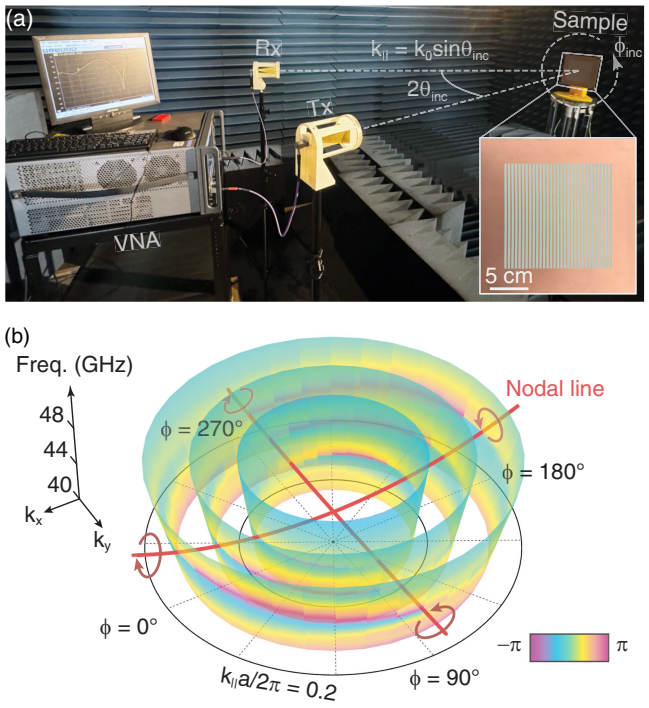

FIG. 3. Experimental observation of nodal lines and their connection to BICs through phase vortices. (a) Experimental setup for angle-resolved metasurface measurement. The fabricated grating sample, made using a PCB, consists of a metallic layer (etched with long rectangular slots) on a dielectric substrate backed by a mirror layer. Source (Tx) and receiver (Rx), each equipped with a quarter-wave plate for circular polarization control, are positioned two meters from the sample in the far-field region. The incident beam is clockwise polarized while the receiver detects counterclockwise-polarized reflection. The reflected field is recorded using a vector network analyzer (VNA) at specific incident lifting angles θ_{inc}. An incident azimuthal angle ϕ_{inc} is varied by rotating the sample mounting rack. The setup is housed in an anechoic chamber to minimize multipath effects and external interferences. The measurement captures the cross-circularly-polarized reflection phase as a function of ϕ_{inc} and frequency ω, enabling phase vortex detection, which serve as signatures of scattering-matrix DPs. (b) Experimental observation of phase behavior in frequency-momentum space. The plotted phase is the argument of the cross-circular polarization reflection coefficient (converting clockwise to counterclockwise circular polarization), the standard quantity measured to reveal geometric phase vortices associated with diabolic points. The 3D phase map reveals nodal lines (light red lines) in ω-k_x-k_y space, with phase vortices observed at azimuthal angles approximately $m \times 90°$. Curved arrows indicate the phase-increasing direction around these vortices. Nodal lines converge at the BIC (located at the Γ point), forming a nodal chain, consistent with the theoretical model.

rack to vary the azimuthal angle ϕ_{inc} and measuring reflected fields using a vector network analyzer (VNA), we mapped a cross-circularly-polarized reflection phase in frequency-momentum space. For comparison with theoretical predictions, the measured incident angles were transformed into the in-plane wave vector $k_{||}$ using the relation $k_{||} = k_0\theta_{inc}$.

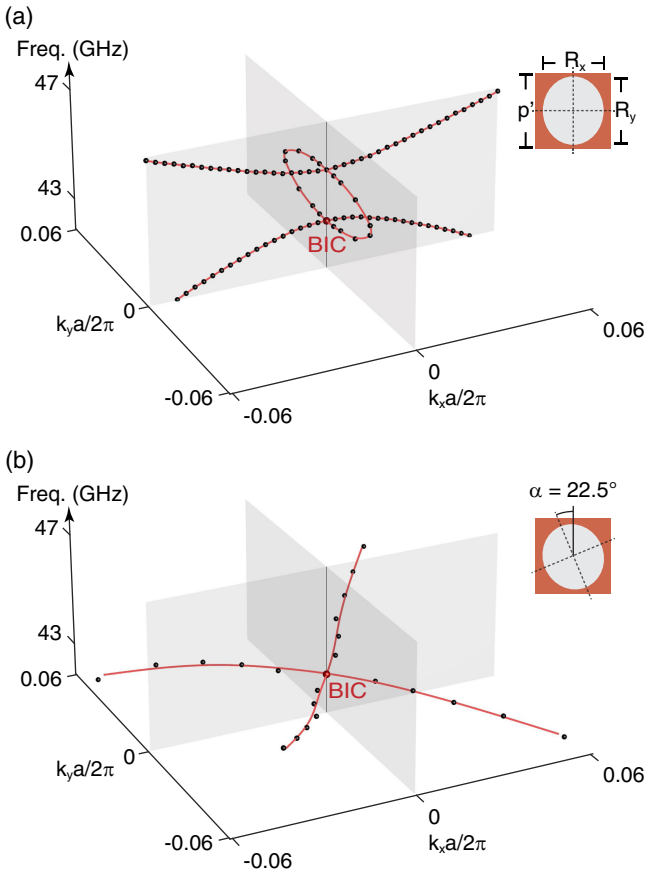

FIG. 4. Effect of breaking mirror symmetry on nodal chain structures and BIC behavior. (a) Inset: schematic of the simulated reflective metasurface structure, designed based on a PCB. The structure consists of a metallic layer (etched with elliptical holes) on a dielectric substrate backed by a mirror layer. The thickness of the dielectric layer is the same as in the grating structure. The metasurface exhibits C_{2v} symmetry when the ellipses are upright, leading to a nodal chain structure in the ω-k_x-k_y space. One of the nodal chain points is a BIC, while the other is a regular diabolic point (or a conventional chain point). (b) To explore whether the nodal chain behavior of the BIC is dependent on mirror symmetry, we rotate the elliptical holes by $\alpha = 22.5°$, breaking the mirror symmetry while retaining C_2 rotational symmetry. Despite the removal of mirror symmetry, the nodal chain point at the BIC remains robust, confirming that the nodal chain pinning behavior of the BIC is a more fundamental phenomenon and is not reliant on mirror symmetry. However, the conventional chain point, which is not protected by the same mechanism, disappears. This demonstrates that the BIC's nodal chain pinning is governed by its singular scattering behavior, not a specific symmetry.

The experimental phase map reveals a clear nodal chain structure [Fig. 3(b)]. Those scattering-matrix nodal lines are experimentally identified through phase vortices in a cross-circularly-polarized reflection coefficient [41], where phase undergoes a continuous 2π winding around

degeneracy points. In our measurements, these characteristic phase vortices appear at azimuthal angles approximately $m \times 90°$, indicated by the curved arrows showing a phase-accumulation direction. These vortices serve as experimental signatures of scattering-matrix DPs. The observed nodal lines (light red) converge at the Γ point where the BIC is located, forming the nodal chain structure predicted by theoretical analysis and numerical simulations. The experimental results demonstrate good agreement with predictions, confirming fundamental connection between BICs and nodal chains in scattering-matrix eigenvalue space.

Robustness against symmetry breaking: Building upon our theoretical framework and simulations, we demonstrate that the physics of BIC-associated nodal chains exhibits remarkable robustness under both geometric modifications and symmetry reduction. We modified our metasurface design by changing rectangular slots to elliptical holes while maintaining PCB-based structure, now with a square lattice (period $a' = 0.35$ cm) and adjusted dielectric thickness ($t' = 0.25$ mm) [Fig. 4(a), inset]. The elliptical holes have major axis $r_a = 0.9a'$ and minor axis $r_b = 0.8a'$. This modified structure, with upright ellipses, preserves C_{2v} symmetry with two perpendicular mirror planes. Figure 4(a) shows the scattering-matrix eigenvalue calculation, revealing a nodal chain with its chain point manifesting as a BIC and another with a conventional chain point, demonstrating the nodal chain pinning phenomenon persists under geometric modifications.

The most striking evidence of the phenomenon's fundamental nature emerges rotating these elliptical holes by $\alpha = 22.5°$. This breaks mirror symmetry while preserving only C_2 rotational symmetry. Our calculations reveal, remarkably, that while the conventional chain point vanishes under this symmetry reduction, the nodal chain point at the BIC remains robust [Fig. 4(b)]. This selective persistence demonstrates nodal chain pinning at BICs transcends both geometric specifics and mirror symmetry protection, instead arising from fundamental singular scattering behavior of the BIC itself. Detailed analysis in Supplemental Material [40], including simulations of off-Γ Friedrich-Wintgen BICs using rigorous coupled-wave analysis (RCWA), demonstrates that C_2 symmetry, with reciprocity and time-reversal symmetry, acts as a global topological constraint rather than merely a local protection mechanism. The robustness traces to BICs' physical nature as zero- bandwidth resonances, guaranteeing a nontrivial 2π eigenphase jump regardless of symmetry conditions—a feature persisting even when mirror symmetry is broken. The fundamental distinction between BIC-pinned and conventional mirror-symmetry-protected chain points appears through eigenvalue difference analysis (see Supplemental Material [40]): BIC points manifest as sudden jumps in eigenphase difference maps, whereas normal chain points show continuous behavior. This suggests the existence of a more sophisticated topological invariant beyond simple Berry phase calculations.

Conclusion—We have uncovered a fundamental connection between BICs and nodal lines in scattering matrix descriptions of electromagnetic systems. We demonstrated that BICs serve as robust pinning points for nodal chains in scattering-matrix eigenvalue space, establishing a new topological perspective on scattering processes. Through theoretical analysis, numerical simulations, and experimental validation using a reflective metasurface platform, we showed this pinning mechanism persists even when structural symmetries break, indicating its origin in the fundamental singular scattering nature of BICs rather than simple symmetry protection.

This discovery bridges two previously distinct areas of topological physics—BICs and nodal lines—through the scattering matrix framework. The robustness of BIC-pinned nodal chains, stemming from intrinsic topological character of zero-bandwidth resonances, suggests potential applications in designing topologically protected optical devices [44] resilient to fabrication imperfections and structural perturbations. This Letter opens several exciting directions for future investigation. Extension to higher-dimensional scattering matrices involving transmission and diffraction channels may reveal non-Abelian singularities characterized by matrix-valued topological invariants [33,45,46]. In transmissive systems, the 4×4 (or higher-dimensional) scattering matrices should preserve fundamental BIC-pinned nodal chain mechanism while enabling richer topological structures. Additionally, these nodal chains' evolution under material loss and parity-time symmetric conditions presents intriguing possibilities for exploring the interplay between non-Hermiticity and topological features in scattering processes [47–53]. In lossy optical systems, material absorption breaks scattering matrix unitarity, fundamentally altering the topological structure. Under loss, nodal chains transform into exceptional lines—non-Hermitian analogs of nodal degeneracies. Although the BIC-pinning mechanism breaks down under loss, the spawned exceptional lines [41] remain localized near original BIC positions, preserving a remnant connection to underlying topological structure. These exceptional lines inherit certain topological properties and exhibit rich chiral polarization structures, opening distinct possibilities for non-Hermitian topological photonics and practical applications such as enhanced sensing. These directions may lead to novel approaches for controlling topologically protected states in photonic systems.

Acknowledgments—W. L. and J. Z. are supported by National Natural Science Foundation of China (No. 12321161645). W. L. and C. T. C. are supported by Hong Kong RGC (No. CRS_HKUST601/23 and No. AoE/P-502/20). Y.-S. Z. and G.-B. W. are supported by the

Research Grants Council of Hong Kong (No. CityU 21207824). The authors would like to thank Professor Meng Xiao, Professor Lei Shi, and Professor Jian Zi for helpful discussions. The authors also thank K. F. Chan of the State Key Laboratory of Terahertz and Millimeter Waves (City University of Hong Kong) for his help in the polarizer and metasurface fixture fabrication.

W. L., G.-B. W., and C. T. C. conceived the idea. W. L., J. Z., R.-Y. Z., X. C., and C. T. C. developed the theoretical framework. W. L. and J. Z. performed simulations. Y.-S. Z., C. Y., and G.-B. W. developed the experimental system and conducted the experimental measurements. W. L. and Y.-S. Z. analyzed experimental data. W. L., Y.-S. Z., G.-B. W., and C. T. C. wrote the manuscript. G.-B. W. and C. T. C. supervised the project. All authors reviewed and provided input on the manuscript.

The authors declare no competing interests.

Data availability—The data that support the findings of this article are not publicly available. The data are available from the authors upon reasonable request.

[1] Y. Plotnik, O. Peleg, F. Dreisow, M. Heinrich, S. Nolte, A. Szameit, and M. Segev, Experimental observation of optical bound states in the continuum, Phys. Rev. Lett. **107**, 183901 (2011).

[2] C. W. Hsu, B. Zhen, J. Lee, S.-L. Chua, S. G. Johnson, J. D. Joannopoulos, and M. Soljačić, Observation of trapped light within the radiation continuum, Nature (London) **499**, 188 (2013).

[3] Y. Yang, C. Peng, Y. Liang, Z. Li, and S. Noda, Analytical perspective for bound states in the continuum in photonic crystal slabs, Phys. Rev. Lett. **113**, 037401 (2014).

[4] K. L. Koshelev, Z. F. Sadrieva, A. A. Shcherbakov, Y. Kivshar, and A. A. Bogdanov, Bound states in the continuum in photonic structures, Usp. Fiz. Nauk **193**, 528 (2021).

[5] L. Huang, Y. K. Chiang, S. Huang, C. Shen, F. Deng, Y. Cheng, B. Jia, Y. Li, D. A. Powell, and A. E. Miroshnichenko, Sound trapping in an open resonator, Nat. Commun. **12**, 4819 (2021).

[6] G. Xu, H. Xing, Z. Xue, D. Lu, J. Fan, J. Fan, P. P. Shum, and L. Cong, Recent advances and perspective of photonic bound states in the continuum, Ultrafast Sci. **3**, 0033 (2023).

[7] B. Jia, L. Huang, A. S. Pilipchuk, S. Huang, C. Shen, A. F. Sadreev, Y. Li, and A. E. Miroshnichenko, Bound states in the continuum protected by reduced symmetry of three-dimensional open acoustic resonators, Phys. Rev. Appl. **19**, 054001 (2023).

[8] L. Huang, L. Xu, D. A. Powell, W. J. Padilla, and A. E. MiroshnichenkojX, Resonant leaky modes in all-dielectric metasystems: Fundamentals and applications, Phys. Rep. **1008**, 1 (2023).

[9] L. Huang, S. Li, C. Zhou, H. Zhong, S. You, L. Li, Y. Cheng, and A. E. Miroshnichenko, Realizing ultrahigh-q resonances through harnessing symmetry-protected bound states in the continuum, Adv. Funct. Mater. **34**, 2309982 (2023).

[10] R. Chai, W. Liu, Z. Li, Y. Zhang, H. Wang, H. Cheng, J. Tian, and S. Chen, Spatial information lasing enabled by full-k-space bound states in the continuum, Phys. Rev. Lett. **132**, 183801 (2024).

[11] F. Wu, X. Qi, M. Qin, M. Luo, Y. Long, J. Wu, Y. Sun, H. Jiang, T. Liu, S. Xiao, and H. Chen, Momentum mismatch driven bound states in the continuum and ellipsometric phase singularities, Phys. Rev. B **109**, 085436 (2024).

[12] Y. Zeng, X. Zhang, X. Ouyang, Y. Li, C. Qiu, Q. Song, and S. Xiao, Manipulating light with bound states in the continuum: From passive to active systems, Adv. Opt. Mater. **12**, 2400296 (2024).

[13] J. Wang, P. Li, X. Zhao, Z. Qian, X. Wang, F. Wang, X. Zhou, D. Han, C. Peng, L. Shi, and J. Zi, Optical bound states in the continuum in periodic structures: Mechanisms, effects, and applications, Photonics Insights **3**, R01 (2024).

[14] B. Zhen, C. W. Hsu, L. Lu, A. D. Stone, and M. Soljačić, Topological nature of optical bound states in the continuum, Phys. Rev. Lett. **113**, 257401 (2014).

[15] H. M. Doeleman, F. Monticone, W. den Hollander, A. Alú, and A. F. Koenderink, Experimental observation of a polarization vortex at an optical bound state in the continuum, Nat. Photonics **12**, 397 (2018).

[16] Y. Zhang, A. Chen, W. Liu, C. W. Hsu, B. Wang, F. Guan, X. Liu, L. Shi, L. Lu, and J. Zi, Observation of polarization vortices in momentum space, Phys. Rev. Lett. **120**, 186103 (2018).

[17] W. Liu, B. Wang, Y. Zhang, J. Wang, M. Zhao, F. Guan, X. Liu, L. Shi, and J. Zi, Circularly polarized states spawning from bound states in the continuum, Phys. Rev. Lett. **123**, 116104 (2019).

[18] Y. Chen, H. Deng, X. Sha, W. Chen, R. Wang, Y.-H. Chen, D. Wu, J. Chu, Y. S. Kivshar, S. Xiao, and C.-W. Qiu, Observation of intrinsic chiral bound states in the continuum, Nature (London) **613**, 474 (2023).

[19] Z.-P. Zhuang, H.-L. Zeng, X.-D. Chen, X.-T. He, and J.-W. Dong, Topological nature of radiation asymmetry in bilayer metagratings, Phys. Rev. Lett. **132**, 113801 (2024).

[20] X. Zhao, J. Wang, W. Liu, Z. Che, X. Wang, C. T. Chan, L. Shi, and J. Zi, Spin-orbit-locking chiral bound states in the continuum, Phys. Rev. Lett. **133**, 036201 (2024).

[21] L. Huang, B. Jia, A. S. Pilipchuk, S. Huang, C. Shen, A. F. Sadreev, Y. Li, and A. E. Miroshnichenko, Merging bound states in the continuum in an open acoustic resonator, Sci. China Phys. Mech. Astron. **68**, 214311 (2024).

[22] B. Wang, W. Liu, M. Zhao, J. Wang, Y. Zhang, A. Chen, F. Guan, X. Liu, L. Shi, and J. Zi, Generating optical vortex beams by momentum-space polarization vortices centred at bound states in the continuum, Nat. Photonics **14**, 623 (2020).

[23] J. Wang, M. Zhao, W. Liu, F. Guan, X. Liu, L. Shi, C. T. Chan, and J. Zi, Shifting beams at normal incidence via controlling momentum-space geometric phases, Nat. Commun. **12**, 6046 (2021).

[24] M. V. Berry and M. Wilkinson, Diabolical points in the spectra of triangles, Proc. R. Soc. A **392**, 15 (1984).

[25] L. Lu, J. D. Joannopoulos, and M. Soljačić, Topological photonics, Nat. Photonics **8**, 821 (2014).

[26] J. Yang, C. Qian, X. Xie, K. Peng, S. Wu, F. Song, S. Sun, J. Dang, Y. Yu, S. Shi, J. He, M. J. Steer, I. G. Thayne, B.-B. Li, F. Bo, Y.-F. Xiao, Z. Zuo, K. Jin, C. Gu, and X. Xu, Diabolical points in coupled active cavities with quantum emitters, Light Sci. Appl. **9**, 6 (2020).
[27] A. A. Burkov, M. D. Hook, and L. Balents, Topological nodal semimetals, Phys. Rev. B **84**, 235126 (2011).
[28] W. Gao, B. Yang, B. Tremain, H. Liu, Q. Guo, L. Xia, A. P. Hibbins, and S. Zhang, Experimental observation of photonic nodal line degeneracies in metacrystals, Nat. Commun. **9**, 950 (2018).
[29] Q. Yan, R. Liu, Z. Yan, B. Liu, H. Chen, Z. Wang, and L. Lu, Experimental discovery of nodal chains, Nat. Phys. **14**, 461 (2018).
[30] L. Xia, Q. Guo, B. Yang, J. Han, C.-X. Liu, W. Zhang, and S. Zhang, Observation of hourglass nodal lines in photonics, Phys. Rev. Lett. **122**, 103903 (2019).
[31] C. H. Lee, A. Sutrisno, T. Hofmann, T. Helbig, Y. Liu, Y. S. Ang, L. K. Ang, X. Zhang, M. Greiter, and R. Thomale, Imaging nodal knots in momentum space through topolectrical circuits, Nat. Commun. **11**, 4385 (2020).
[32] H. Park, W. Gao, X. Zhang, and S. S. Oh, Nodal lines in momentum space: Topological invariants and recent realizations in photonic and other systems, Nanophotonics **11**, 2779 (2022).
[33] D. Wang, Y. Wu, Z. Q Zhang, and C.T Chan, Non-abelian frame charge flow in photonic media, Phys. Rev. X **13**, 021024 (2023).
[34] J.-W. Liu, F.-L. Shi, K. Shen, X.-D. Chen, K. Chen, W.-J. Chen, and J.-W. Dong, Antichiral surface states in time-reversal-invariant photonic semimetals, Nat. Commun. **14**, 2027 (2023).
[35] H. Qiu, Y. Li, Q. Zhang, and C. Qiu, Discovery of higher-order nodal surface semimetals, Phys. Rev. Lett. **132**, 186601 (2024).
[36] W. Liu, H. Wang, B. Yang, and S. Zhang, Correspondence between euler charges and nodal-line topology in Euler semimetals, Sci. Adv. **11**, eads5081 (2025).
[37] S. Coleman and J. Mandula, All possible symmetries of the s matrix, in *Dynamical Groups and Spectrum Generating Algebras*, Vol. 159 (World Scientific, Singapore, 1988), pp. 469–474.
[38] P. C. Waterman, Symmetry, unitarity, and geometry in electromagnetic scattering, Phys. Rev. D **3**, 825 (1971).
[39] Z. Zhao, C. Guo, and S. Fan, Connection of temporal coupled-mode-theory formalisms for a resonant optical system and its time-reversal conjugate, Phys. Rev. A **99**, 033839 (2019).
[40] See Supplemental Material at http://link.aps.org/supplemental/10.1103/rpb2-ryyk for detailed theoretical derivations of scattering matrix symmetry constraints; additional simulations on all-dielectric metasurfaces, off-Γ BICs demonstrating global C_2 symmetry protection, eigenvalue phase difference analysis, and nodal chain robustness in C_2-symmetric systems without mirror symmetry; and experimental details including circularly polarized antenna design.
[41] J. Chen, W. Liu, J. Wang, C. Li, R.-Y. Zhang, X. Cui, F. Guan, L. Shi, J. Zi, and C. T. Chan, Continuous lines of topological singularities in metasurface scattering matrices: From nodal to exceptional, ACS Photonics **12**, 3208 (2025).
[42] S.-W. Wang, C.-H. Chien, C.-L. Wang, and R.-B. Wu, A circular polarizer designed with a dielectric septum loading, IEEE Trans. Microwave Theory Tech. **52**, 1719 (2004).
[43] K. X. Wang and H. Wong, A wideband millimeter-wave circularly polarized antenna with 3-d printed polarizer, IEEE Trans. Antennas Propag. **65**, 1038 (2017).
[44] Y. Guo, M. Xiao, and S. Fan, Topologically protected complete polarization conversion, Phys. Rev. Lett. **119**, 167401 (2017).
[45] Q. Wu, A. A. Soluyanov, and T. Bzdušek, Non-Abelian band topology in noninteracting metals, Science **365**, 1273 (2019).
[46] Y. Yang, B. Yang, G. Ma, J. Li, S. Zhang, and C. T. Chan, Non-Abelian physics in light and sound, Science **383**, eadf9621 (2024).
[47] S. Longhi, Pt-symmetric laser absorber, Phys. Rev. A **82**, 031801(R) (2010).
[48] Y. D. Chong, L. Ge, and A. D. Stone, Pt-symmetry breaking and laser-absorber modes in optical scattering systems, Phys. Rev. Lett. **106**, 093902 (2011).
[49] M. Lawrence, N. Xu, X. Zhang, L. Cong, J. Han, W. Zhang, and S. Zhang, Manifestation of pt symmetry breaking in polarization space with terahertz metasurfaces, Phys. Rev. Lett. **113**, 093901 (2014).
[50] Q. Song, M. Odeh, J. Zúñiga-Pérez, B. Kanté, and P. Genevet, Plasmonic topological metasurface by encircling an exceptional point, Science **373**, 1133 (2021).
[51] Y. Xu, L. Li, H. Jeong, S. Kim, I. Kim, J. Rho, and Y. Liu, Subwavelength control of light transport at the exceptional point by non-Hermitian metagratings, Sci. Adv. **9**, eadf3510 (2023).
[52] T. He, Z. Zhang, J. Zhu, Y. Shi, Z. Li, H. Wei, Z. Wei, Y. Li, Z. Wang, C.-W. Qiu, and X. Cheng, Scattering exceptional point in the visible, Light Sci. Appl. **12**, 229 (2023).
[53] J. Erb, N. Shaibe, R. Calvo, D. P. Lathrop, T. M. Antonsen, T. Kottos, and S. M. Anlage, Topology and manipulation of scattering singularities in complex non-hermitian systems: Two-channel case, Phys. Rev. Res. **7**, 023090 (2025).

End Matter

Methods—Simulations and determination of diabolic points: Eigenmode and scattering matrix simulations were conducted using a finite-element method. The simulation domain consists of a square unit cell comprising an air pillar, a single unit cell of the metasurface (grating) backed by a metallic layer. The metallic strips and layer are simplified by applying a perfect electric conductor boundary condition. Periodic (Bloch) boundary conditions were applied along the x and y directions to model the infinite periodic structure,

while perfect matching layers were implemented in the $+z$ direction to simulate an open boundary.

For eigenmode simulations, no external source was introduced, and only the eigenfrequencies of the system were solved. On the other hand, for scattering matrix simulations, plane-wave sources were applied with periodic ports to excite the system at different frequencies and different incident angles. To fully characterize the scattering matrix, two independent simulations were performed for each incident angle, corresponding to orthogonal incident polarizations p and s, so that the reflection coefficients $r_{pp}, r_{sp}, r_{ss}, r_{ps}$ can be obtained.

To determine the position of DPs in the frequency-momentum space so that we can map out the nodal lines and chains, we first perform scattering simulations sweeping k_x and ω with different fixed values of k_y. In each ω-k_x map, we then calculate the eigenvalues and obtain their differences as a map. The zero points in these difference maps represent diabolic points, and connecting them gives the nodal lines.

Sample measurements: The experimental characterization of the metasurface sample is performed in an anechoic chamber to minimize external electromagnetic interference and unwanted reflections. The experimental setup consists of a transmitting (Tx) horn antenna, a receiving (Rx) horn antenna, two polarizers, and a vector network analyzer (VNA, Keysight PNA 5227B). The horn antennas are connected to the two ports of the VNA via 50-Ω coaxial cables. To achieve circular polarization, two wideband 3D-printed polarizers are positioned on the apertures of the horn antennas, effectively converting the linearly polarized waves emitted by the antennas into circularly polarized waves. Detailed information on the polarizer design is provided in Supplemental Material [40]. The metasurface reflections are recorded by measuring the S21 parameter on the VNA. The frequency range for measurements spans from 35 to 50 GHz. To suppress the noise floor, the VNA's intermediate frequency bandwidth is set to 200 Hz. Both the Tx and Rx antennas are placed two meters away from the metasurface to ensure uniform plane wave illumination across the measured frequency range. Before characterizing the metasurface, a plain PCB metal plate with identical dimensions is measured, and its data serves as the reference phase. Subsequently, the metasurface reflections are recorded, and the experimental phase map is obtained by subtracting the raw phases of the metasurface from those of the plain PCB plate.